Structure of Poly(dimethylsiloxane) Melts: Theory, Simulation, and Experiment

Scott W. Sides*

Sandia National Laboratories, Albuquerque, New Mexico 87185, and Department of Chemical Engineering, University of California, Santa Barbara, California 93106

John Curro, Gary S. Grest, and Mark J. Stevens

Sandia National Laboratories, Albuquerque, New Mexico 87185

Thomas Soddemann

Department of Physics and Astronomy, Johns Hopkins University, Baltimore, Maryland 21218

A. Habenschuss

Oak Ridge National Laboratory, Oak Ridge, Tennessee 37831

J. D. Londono

E.I. Dupont, Experimental Station Laboratory, ESL 323-109B, Wilmington, Delaware 19880

Received May 20, 2002

ABSTRACT: Molecular dynamics simulations, integral equation theory, and wide-angle X-ray scattering experiments are used to study the structure of a poly(dimethylsiloxane) (PDMS) melt. Two different chain models are employed for the molecular dynamics: a united-atom class I potential and an explicit-atom class II potential. The effects of partial charges and attractions on the intermolecular pair correlation functions are studied for the united atom model. Good qualitative agreement between the polymer reference interaction site model (PRISM theory) and the simulations is found for the united atom model with charges and attractive dispersion interactions turned off. Simulation results for both the united-atom and explicit-atom models for the structure factor are in excellent agreement with the X-ray scattering measurements for high wavevector. However, the explicit-atom model gives significantly better agreement for low wavevector, particularly in the vicinity of the first peak.

I. Introduction

Silicone polymers have several characteristics that make them very useful for engineering applications. For example, because of the high degree of flexibility of the polymer backbone, poly(dimethylsiloxane) (PDMS) has the lowest glass transition temperature (~150 K) of any known polymer. Because of its high degree of chemical stability, PDMS is also functional at relatively high temperatures. For these reasons, materials based on PDMS are ideal for applications such as elastomeric seals, adhesives, coatings, and encapsulants. In these applications PDMS exists in the bulk amorphous state as a liquid or as a cross-linked network. The purpose of the present investigation is to (1) measure the wide-angle X-ray scattering (WAXS) structure factor of PDMS, (2) model the structure and packing of PDMS in the liquid state through molecular dynamics (MD) simulations and polymer reference interaction site model (PRISM) calculations, and (3) compare the results of theory, simulation, and experiment.

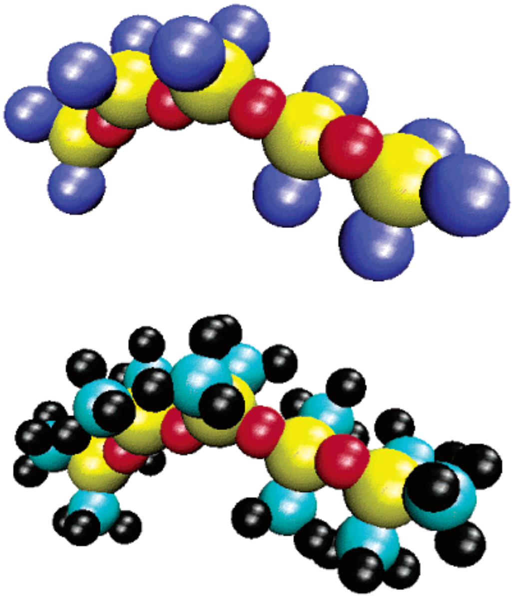

Figure 1. (top) United-atom (UA) model for PDMS: yellow (Si), red (O), blue (CH_3). (bottom) Explicit-atom (EA) model for PDMS: yellow (Si), red (O), cyan (C), black (H). These chains with 5 Si per chain are for illustration purposes. The chain length used in the MD and PRISM studies is longer, 20 Si per chain. (Note: relative sizes of atoms not to scale.)

The molecular structure of PDMS is shown in Figure 1. Note that the PDMS chain is similar in architecture to poly(isobutylene) (PIB), with the CH_2 group replaced by O and the C by Si. In PIB the macromolecules are known to pack very densely, which results in an extraordinarily low diffusion constant for gases in PIB elastomers. PIB and other polyolefins were modeled previously[1,2] through MD simulations and PRISM theory

---

* To whom correspondence should be addressed at UC Santa Barbara.

10.1021/ma020014k CCC: $22.00

and also studied with WAXS.[2] PDMS, on the other hand, has a relatively low density and high diffusivity for gases. This is primarily a consequence of the larger Si−O and Si−C bond lengths compared to the C−C bond length. In addition, the Si−O−Si bond angle in PDMS is larger than the tetrahedral C−C−C bond angle in PIB.

In the simulations, two force fields are used: class I potential of Sok and Berendsen[3] and class II potential of Sun, Rigby, and others.[4−8] The class I potential is implemented in a united-atom (UA) model for which the Si and O atoms are treated explicitly while each methyl group (CH_3) is treated as a single particle. The united-atom potential was used to study the transport of small molecules in PDMS and was not optimized to give the correct structure for a bulk liquid. The class II potential is implemented in an explicit-atom (EA) model which treats the Si, O, C, and H atoms individually. The explicit-atom potential has been optimized to reproduce experimental data describing molecular conformations/energetics, bulk density, and pressure for PDMS. Throughout the rest of this paper, the united-atom model with a class I potential and the explicit-atom model with a class II potential will be referred to as UA/CI and EA/CII, respectively. Our aim in this work is to test the adequacy of these force fields in describing PDMS by comparing the MD simulations with the experimental density and structure factor. Moreover, we also assess the accuracy of PRISM theory in describing PDMS by comparing theory and simulation.

II. Method

Thermodynamic and structural data for PDMS are compared from three sources: theoretical (PRISM), computational (MD), and experimental (WAXS). PRISM theory uses a single-chain Monte Carlo simulation to determine the single-chain structure factor which is used to calculate the intermolecular structure factor for a dense, many-chain system. Molecular dynamics simulations solve Newton's equations for a system of particles from which the structure factor may be calculated directly. Both PRISM and MD calculations use models for PDMS that include functional forms of the classical force fields describing interactions between the atoms or groups of atoms. All PRISM calculations presented here use UA/CI. The MD simulations use both UA/CI and EA/CII. Schematic diagrams of the two models are shown in Figure 1.

Comparing theory, simulation, and experiment allows two issues to be addressed: what are the effects of approximations used in PRISM, and how effective are classical potentials in predicting the structure of PDMS in the liquid state? The approximations in PRISM, made so the theory is tractable, can be tested by MD simulation. With simulations it is possible to adjust the model parameters such that the conditions match those used in the PRISM calculations. These adjustments include testing the importance of the Coulombic interactions on the local packing by comparing simulations with and without charges present. By comparing those results with simulation data using the full interactions, it is possible to evaluate what effect the approximations have on PRISM theory predictions. Also, MD simulations make it possible to calculate the structure of PDMS, using the more sophisticated potentials of the EA/CII model, to make quantitative comparisons to the structure factors obtained from WAXS experiments.

A. PRISM. The polymer reference interaction site model or PRISM theory was developed several years ago by Curro and Schweizer[9−11] as an extension of the RISM theory of Chandler and Andersen.[12,13] PRISM theory has been discussed in detail in previous publications[14,15] and, therefore, will only be described briefly here. The advantage of PRISM over the full MD simulation is that significantly smaller computational resources are required and, therefore, can be applied to much longer chain systems. The tradeoff is that the results are approximate.

The theory represents the polymer chains as a collection of overlapping interaction sites as seen in Figure 1. We begin by assuming that the macromolecules are long so that end effects can be neglected[11] and that all monomers along the chain backbone are equivalent. The goal of the PRISM approach is to calculate the intermolecular pair correlation functions $g_{\alpha\gamma}(r)$ between sites making up the monomers on different chains,

$$g_{\alpha\gamma}(\mathbf{r}) = \int \frac{\langle \rho_\alpha(\mathbf{r}')\,\rho_\gamma(\mathbf{r}-\mathbf{r}')\rangle}{\rho_\alpha\rho_\gamma}\,\mathrm{d}\mathbf{r}' \qquad (1)$$

where ρ_α is the density of sites α. The starting point of the theory is the generalized Ornstein−Zernike equation,[12−15] written for convenience in Fourier space as

$$\hat{\mathbf{h}}(k) = \hat{\Omega}(k)\,\hat{\mathbf{C}}(k)[\hat{\Omega}^{\mathrm{T}}(k) + \rho\hat{\mathbf{h}}(k)] \qquad (2)$$

where the caret denotes Fourier transformation with wave vector $\vec{k}$, ρ is the diagonal matrix of site densities, $\hat{\mathbf{C}}(k)$ is the direct correlation function, and $\hat{\Omega}(k)$ is the single-chain structure factor,

$$\hat{\Omega}_{\alpha\gamma}(k) = \frac{1}{N}\sum_{i\in\alpha j\in\gamma}^{N}\left\langle\frac{\sin kr_{ij}}{kr_{ij}}\right\rangle \qquad (3)$$

Equation 2 relates the average intermolecular packing and intramolecular structure characterized by $h_{\alpha\gamma}(r) = g_{\alpha\gamma}(r) - 1$ and $\hat{\Omega}_{\alpha\gamma}(k)$, respectively. The summation in eq 3 is over intramolecular pairs of sites on a single chain, having N monomers.

The generalized Ornstein−Zernike equation can be viewed as a definition for the intermolecular direct correlation function $C_{\alpha\gamma}(r)$.[14,15] It can be demonstrated from simulation or experiment that at high density the direct correlation function is a short-range function of r. This motivates us to make use of the well-known Percus−Yevick (PY) approximate closure from the theory of atomic liquids[16]

$$C_{\alpha\gamma}(r) \cong \{1 - \exp[\beta U_{\alpha\gamma}(r)]\}[h_{\alpha\gamma}(r) + 1] \qquad (4)$$

where $U_{\alpha\gamma}(r)$ is the nonbonded potential which we take to be of the Lennard-Jones form, $\beta = 1/k_BT$, where k_B is the Boltzmann constant and T is the temperature. Equation 4 can be used to eliminate the direct correlation function from eq 2, thus providing a direct relationship between the intermolecular packing and intramolecular structure of the polymer liquid. It is well-known for atomic liquids[16] that the packing at high density is primarily determined from the repulsive part of the potential. Later in this paper we will test this hypothesis for PDMS liquids using MD simulation. It has been demonstrated previously[14,15] that PRISM theory works best for repulsive potentials; hence, we follow Weeks, Chandler, and Andersen[17] by dividing the

Lennard-Jones potential between nonbonded monomers into a repulsive part $U^{\mathrm{rep}}_{\alpha\gamma}(r)$

$$U^{\mathrm{rep}}_{\alpha\gamma}(r) = \begin{cases} 4\epsilon_{\alpha\gamma}\left[\left(\frac{\sigma_{\alpha\gamma}}{r}\right)^{12} - \left(\frac{\sigma_{\alpha\gamma}}{r}\right)^{6} + \frac{1}{4}\right] & r \le \sigma_{\alpha\gamma}2^{1/6} \\ 0 & r > \sigma_{\alpha\gamma}2^{1/6} \end{cases} \qquad (5)$$

and an attractive or perturbative contribution $U^{\mathrm{att}}_{\alpha\gamma}(r)$

$$U^{\mathrm{att}}_{\alpha\gamma}(r) = \begin{cases} -\epsilon_{\alpha\gamma} & r < \sigma_{\alpha\gamma}2^{1/6} \\ 4\epsilon_{\alpha\gamma}\left[\left(\frac{\sigma_{\alpha\gamma}}{r}\right)^{12} - \left(\frac{\sigma_{\alpha\gamma}}{r}\right)^{6}\right] & r \ge \sigma_{\alpha\gamma}2^{1/6} \end{cases} \qquad (6)$$

In the present investigation of PDMS, we will employ only the repulsive part of the potential in the closure relation in eq 4. The PRISM theory outlined here has been applied previously to polyolefin melts[1,2] and blends.[18,19] In the present application to PDMS melts, each monomer contains three independent, united atom sites representing O, Si, and CH_3 moieties. Thus, the matrices in eq 2 are of size 3 × 3, and there are six independent $g_{\alpha\gamma}(r)$ needed to characterize the PDMS melt within the united atom model.

For a given intramolecular structure function $\hat{\Omega}_{\alpha\gamma}(k)$, eqs 2 and 4 can be solved numerically for the intermolecular radial distribution functions. As a first approximation, one could use Flory's hypothesis[14,15,20] by approximating the single chain structure in a polymer melt as a chain without long-range excluded-volume interactions. More exact calculations on flexible chains, however, require that the intramolecular structure be determined self-consistently with the intermolecular packing.[1,2,14,15] This self-consistent computation proceeds by replacing the full many chain computation with a single chain Monte Carlo simulation in the potential energy field

$$U(\mathscr{R}) = U_{\mathrm{E}} + W(\mathscr{R}) \qquad (7)$$

where U_{E} represents the conventional bonded and nonbonded interactions that an isolated chain would experience. $W(\mathscr{R})$ is a medium-induced potential that mimics the effects of the other chains in the system and depends on their configurations $\mathscr{R}$. The essence of the Flory hypothesis is that the repulsive excluded-volume interactions and attractive medium induced potentials effectively cancel each other in eq 7. In this work we approximate this medium-induced potential as being pairwise additive with the form[14,15,21,22]

$$\beta\hat{W}_{\alpha\gamma}(k) = -\sum_{i,j}\hat{C}_{\alpha i}(k)\,\hat{S}_{ij}(k)\,\hat{C}_{j\gamma}(k) \qquad (8)$$

where the partial structure factors are defined as

$$\hat{S}_{\alpha\gamma}(k) = \rho_\alpha\hat{\Omega}_{\alpha\gamma}(k) + \rho_\alpha\rho_\gamma\hat{h}_{\alpha\gamma}(k) \qquad (9)$$

Since the medium-induced potential depends on the intermolecular direct correlation functions, it is necessary to solve the self-consistent problem iteratively. One begins by guessing $W_{\alpha\gamma}(r)$ in eq 7. A single chain Monte Carlo simulation is then performed with the potential U to obtain the single chain structure function defined in eq 3. This intramolecular structure function $\hat{\Omega}_{\alpha\gamma}(k)$ is then used as input to PRISM theory where eqs 2 and 4 are solved for the direct correlation functions. This leads to a new estimate for the medium-induced potential through eqs 8 and 9. The procedure is then repeated until the medium-induced potential does not change from one iteration to the next within some tolerance. At this point we have converged to a self-consistent solution for both the intramolecular structure and intermolecular packing. It is important to note that reweighting techniques are employed so that the Monte Carlo simulation does not have to be repeated in each iteration.[1]

B. Molecular Dynamics. All simulation data are obtained from systems containing 100 chains of 20 Si atoms per chain, except one system of 800 chains using only the UA/CI model neglecting Coulomb interactions. Class I potentials include terms describing the interactions due to nonbond, bond, angle, and torsional forces. Nonbond forces arise from van der Waals and Coulombic interactions between all particles on different chains and between particles on the same chain which are farther apart than fourth or third-nearest neighbors for class I and class II potentials, respectively. Bond, angle, and torsional terms arise from intrachain connectivity. The bond potential describes the strong, two-body, covalent interactions that define which atoms belong to each PDMS molecule. The angular potential describes three-body interactions which allow for chain stiffness. The torsional potential describes four-body interactions and enforces an energetic penalty for twisting motion about bonds along each chain. The functional forms and parameters of the class I potential are given elsewhere.[3] The class II potential contains all terms from the class I potential plus additional cross-term interactions. The exact functional forms of the class II potential are different from class I and include more anharmoncity in the interactions. The nonzero cross-terms used in this study of PDMS are bond−bond and bond−angle interactions. Extensive discussions about derivation of the functional forms and optimization of parameters used by the class II potentials can be found elsewhere.[4−8]

For selected UA/CI simulations the nonbond interactions are adjusted in order to evaluate their effects on thermodynamic and structural properties. Therefore, the functional forms of the LJ and Coulombic potentials are shown below. The nonbond potential for both class I and class II is defined as

$$U^{\mathrm{nonbond}}_{\alpha\gamma}(r) = \begin{cases} U^{\mathrm{vW}}_{\alpha\gamma}(r) + k_q\dfrac{q_\alpha q_\gamma}{r} & r < r_{\mathrm{c}} \\ k_q\dfrac{q_\alpha q_\gamma}{r} & r > r_{\mathrm{c}} \end{cases} \qquad (10)$$

where q is the electric charge, r is the distance between any two atoms $i-j$ of type $\alpha-\gamma$, respectively, and r_{c} is the cutoff on the van der Waals interaction. The proportionality constant for the electrostatic potential energy is $k_q = 1/(4\pi\epsilon_0) = 332.06(\mathrm{kcal\ Å})/(e^2\ \mathrm{mol})$ where e is the electron charge. For the full potential including attractive LJ interactions, $r_{\mathrm{c}} = 12.0$ Å for both the UA/CI and EA/CII simulations. The values of r_{c} used in the purely repulsive UA/CI simulations are shown in Table 1. The long-range Coulomb interactions are calculated with a particle−particle/particle−mesh Ewald (PPPM) algorithm.[23] The LJ mixing rules for the class I potential are given by Berthelot mixing rules, while the class II potential employs special LJ mixing rules.[5]

Table 1. Nonbonded Simulation Parameters for the PDMS UA/CI Model[3] [a]

	Si	O	CH_3
ϵ [kcal/mol]	0.5848	0.2049	0.1799
σ [Å]	3.3850	2.955	3.786
q [e]	0.3	−0.3	0.0
r_c^{repl} [Å]	3.799	3.316	4.249
d [Å]	3.44	2.87	3.66

[a] Si atoms located on chain ends have partial charges adjusted in order to preserve overall charge neutrality. d is the effective hard-core diameter.[17]

Table 2. Nonbonded Simulation Parameters for the PDMS EA/CII Model[a]

	Si	O	C	H
ϵ [kcal/mol]	0.131	0.080	0.0620	0.0230
σ [Å]	4.290	3.300	3.8540	2.8780
q [e]	0.7150	−0.4450	−0.2940	0.0530

[a] All other parameters can be found in the literature.[4−8]

The van der Waals potential energy $U^{vW}(r)$ for class I/class II is

$$U_{\alpha\gamma}^{vW}(r) = \begin{cases} 4\epsilon_{\alpha\gamma}\left[\left(\frac{\sigma_{\alpha\gamma}}{r}\right)^{12} - \left(\frac{\sigma_{\alpha\gamma}}{r}\right)^{6}\right] & \text{class I} \\ \epsilon_{\alpha\gamma}\left[2\left(\frac{\sigma_{\alpha\gamma}}{r}\right)^{9} - 3\left(\frac{\sigma_{\alpha\gamma}}{r}\right)^{6}\right] & \text{class II} \end{cases} \tag{11}$$

where σ and ϵ determine the length/energy scales, respectively. All parameters used in the nonbond interactions for the UA/CI and EA/CII potentials are summarized in Tables 1 and 2, respectively.

To initialize the starting configurations, a single, methyl-terminated PDMS molecule is constructed with alternating trans−gauche conformations every fourth oxygen atom to prevent a highly nonequilibrium backfolded structure. The configuration of this PDMS molecule is then copied and the center-of-mass placed in a random location within the simulation box. The molecule is also rotated about its center-of-mass in a random direction. The resulting overlaps among atoms are then removed by running the MD simulation with a soft, nonbond potential until the full nonbond interactions may be switched on safely. A time step of Δt = 0.4 fs is used for most of the simulations. A multiple-time step integrator (RESPA) is used in all simulations such that forces are calculated for: bonded interactions every time step, three- and four-body forces every 2 time steps, and LJ and Coulomb forces every 4 time steps. Simulations using the UA/CI model are run at two densities: $\rho = 0.98$ g/cm^3 and $\rho = 1.01$ g/cm^3. Simulations using the EA/CII model are run at three densities: $\rho = 0.95$ g/cm^3, $\rho = 0.98$ g/cm^3, and $\rho = 1.01$ g/cm^3.[24] A Nose-Hoover thermostat is used to control the temperature T, with a coupling frequency chosen to be 0.02 fs^{-1}. The systems of 100 chains were run on between 16 and 32 processors on the Sandia Cplant clusters. The systems were equilibrated for up to ∼4.0 ns, and statistics were collected for up to ∼5.6 ns sampling configurations every ∼0.08 ns.

C. Experiment. PDMS is a clear viscous liquid with a density of 0.98 g/cm^3 at 25 °C (obtained from Aldrich).[25] The molecular weight given by the manufacturer is 65 000 g/mol as determined from viscosity. The PDMS is used as received, and the X-ray intensities were measured from the free, horizontal surface of the sample, mounted on a Scintag PAD-X diffractometer using reflection geometry.[26] Mo Kα radiation ($\lambda = 0.7107$ Å, 50 kV, 40 mA) and a solid-state detector are used. Intensities are measured over a momentum transfer range of $0.3 < k < 16$ Å^{-1}, where $k = 4\pi\lambda^{-1} \sin\theta$, with 2θ the scattering angle. Sufficient counts are accumulated at each point to keep the statistical error in the k-weighted structure factor (defined below) approximately uniform over the whole momentum transfer range. This entailed collecting well over 10^6 counts at the highest k values where the intensities are lowest.

The measured intensities $I(k)$ are converted to the differential scattering cross sections $d\sigma/d\Omega$[27] by

$$\frac{d\sigma}{d\Omega} = \frac{I(\theta)}{\alpha(\theta)} - \delta(\theta) \tag{12}$$

where $\alpha(\theta)$ depends on the sample and scattering geometry, polarization, and absorption, and $\delta(\theta)$ represents the multiple scattering and incoherent scattering. Accordingly, the measured intensities were corrected for polarization, absorption,[28] incoherent scattering,[29] monochromator discrimination,[30] and multiple scattering.[31] The $d\sigma/d\Omega$ is related to the static coherent scattering function $S(k)$

$$\frac{d\sigma}{d\Omega} = N_T S(k) \tag{13}$$

where N_T is the total number of sites (Si, O, CH_3) in the sample. The corrected X-ray intensities in arbitrary units can be converted to absolute units of electrons per site by normalizing to the self-scattering from uncorrelated sites, $S_{self}(k)$.

$$S_{self}(k) = \sum_{i=1}^{n_s} x_i b_i^{\,2}(k) \tag{14}$$

where n_s is the number of types of sites within a repeat unit, and x_i and $b_i(k)$ are the mole fraction and coherent scattering factors, respectively, of the sites. The coherent scattering factors for Si and O were taken from the International Tables for X-ray Crystallography.[32] For CH_3, we use group scattering factors[33] which treat CH_3 as a single scattering site. Such an analysis gives no information on interactions involving hydrogen, which are hard to obtain due to the low scattering power of hydrogen for X-rays. The normalized static coherent scattering function $S(k)$ and the self-scattering $S_{self}(k)$ for PDMS at 25 °C are shown in Figure 2.

The total structure factor $H(k)$, containing the structurally sensitive part of the data, is defined as

$$H(k) = M(k)[S(k) - S_{self}(k)] \tag{15}$$

where the modification function $M(k)$ is given by

$$M(k) = \left[\sum_{i=1}^{n_s} x_i b_i(k)\right]^{-2} \tag{16}$$

The intensities measured at low angles in reflection mode (below $k \sim 0.5$ Å^{-1}) are very sensitive to scattering geometry and cannot be measured accurately. To obtain the low angle $H(k)$, we rely on the thermodynamic property that the total structure factor at $k = 0$, $H(0)$,

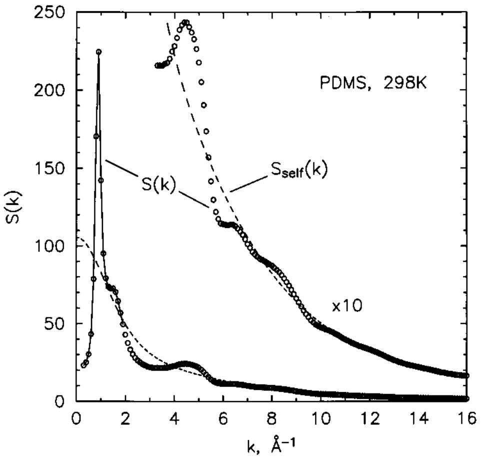

Figure 2. Structure factor data $S(k)$ for PDMS from WAXS experiment at $T = 298$ K. The circles and dashed line denote the scattering data and the self-scattering contribution $S_{\mathrm{self}}(k)$, respectively. The data labeled ×10 has been multiplied by a factor of 10 to magnify the structural details at intermediate to high values of k.

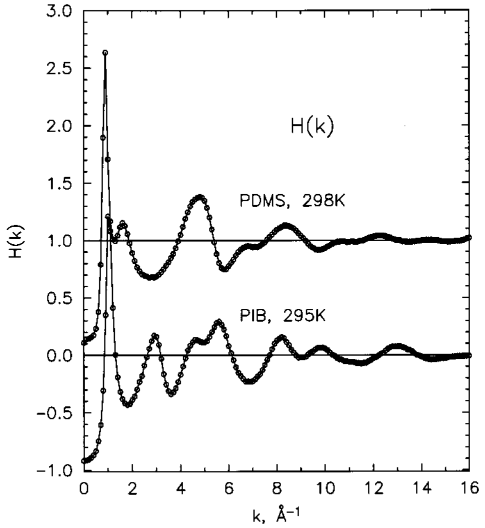

Figure 3. Total structure factor $H(k)$ for PDMS and PIB. The curve for PDMS is offset for clarity.

is related[34] to the bulk isothermal compressibility κ_T through

$$H(0) = k_B \rho T \kappa_T - 1 \tag{17}$$

We used this property to extrapolate $H(k)$ to $H(0)$ from $k \sim 0.5$ Å^{-1}. The experimental site number density is $\rho = 0.031\ 84$ Å^{-3}, and the compressibility ($\kappa_T = 0.001\ 014$ MPa^{-1}) for PDMS is obtained from *PVT* data in the literature,[35] which gives $H(0) = -0.8671$. The total structure factor for PDMS is shown in Figure 3 along with the PIB structure factor for comparison.

III. Simulation Results

The calculation of the $g_{\alpha\gamma}(r)$ functions from PRISM uses a nonbond potential $U_{\alpha\gamma}(r)$ that includes only the repulsive part of a Lennard-Jones potential and ignores the long-range Coulomb interactions. To compare MD and PRISM, as well as test the accuracy of the UA/CI potential for PDMS, simulations are run with/without LJ attractions and with/without Coulomb interactions. The six intermolecular correlation functions for the PDMS UA/CI model are shown in Figure 4, which are calculated directly using the particle positions from MD simulation and averaged over independent configurations. Of the three sets of data shown in Figure 4, the first (open squares) is obtained without Coulomb interactions and a cutoff r_c^{repl} (see Table 1) such that the van der Waals forces are purely repulsive. For the second set of data (filled squares), $U_{\alpha\gamma}^{\mathrm{nonbond}}(r)$ includes van der Waals potential including attractive interactions ($r_c = 12.0$ Å) but no Coulomb interactions. For the third set of data, $U_{\alpha\gamma}^{\mathrm{nonbond}}(r)$ includes both the attractive van der Waals and Coulomb interactions. The intermolecular correlation functions measure local structure and should be dominated by short-range repulsive forces. The data of Figure 4 confirm this assumption as the gross features of the $g_{\alpha\gamma}(r)$'s are insensitive to changes in either the attractive LJ or long-range Coulomb interactions. However, small differences in the $g_{\alpha\gamma}(r)$'s appear due to changes in the nonbond interactions. For all six correlation functions, including the attractive LJ interaction shifts the first $g_{\alpha\gamma}(r)$ peak to smaller r and/or increases first peak height. Including Coulomb interactions enhances these effects further. In particular, Coulomb forces have a relatively large effect on the $g_{\mathrm{O,CH_3}}(r)$ and $g_{\mathrm{O,O}}(r)$ functions where the first peak around 4−5 Å is significantly more pronounced.

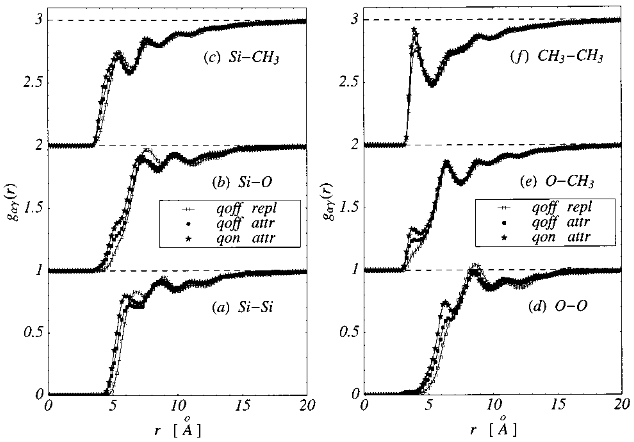

Figure 4. Intermolecular correlation functions $g_{\alpha\gamma}(r)$ calculated by MD simulations using the UA/CI model for PDMS. For all data $T = 300$ K and $\rho = 0.98$ g/cm^3. Symbols denote Coulomb interactions off and repulsive LJ (open squares), Coulomb interactions off and attractive LJ (filled squares), and Coulomb interactions on and attractive LJ (filled stars). Each function is normalized such that $g_{\alpha\gamma}(r) \to 1$ as $r \to \infty$. The values for the $g_{\alpha\gamma}(r)$ functions in each panel have been offset for clarity.

It is instructive to compare the intermolecular correlations for PDMS in Figure 4 with previous results[1] on PIB melts. Qualitatively, the $g_{\alpha\gamma}(r)$ functions are similar for the two polymers with the methyl−methyl correlations having a large peak at short distances reflecting the fact that intermolecular CH_3 groups can approach each other readily in the liquid. Likewise, intermolecular correlations between backbone sites are screened by the pendant methyl substituents in both PDMS and PIB. However, more structure is observed in PDMS for the short-range correlations between backbone sites, particularly for $g_{\alpha\gamma}(r)$ between Si− CH_3, O−O, and O−CH_3. This is a consequence of the larger bond lengths and angles in PDMS, resulting in less screening due to the presence of the methyl groups. It can also be seen in Figure 4 that the partial charges induce additional short-range structure as seen in the O−O and O−CH_3 correlations.

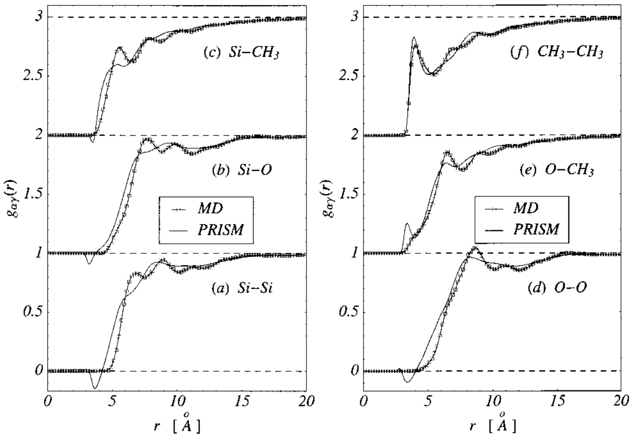

Figure 5. Comparison of intermolecular correlation function $g_{\alpha,\gamma}(r)$ as calculated from PRISM theory (solid line) and MD simulation using the UA/CI model (points). The MD data are for the case without Coulomb interactions and only repulsive LJ interactions, affording the most direct comparison with PRISM. For all data $\rho = 0.98$ g/cm^3. Because of numerical errors in evaluating PRISM theory, some of the $g_{\alpha,\gamma}(r)$ functions have spurious negative values.

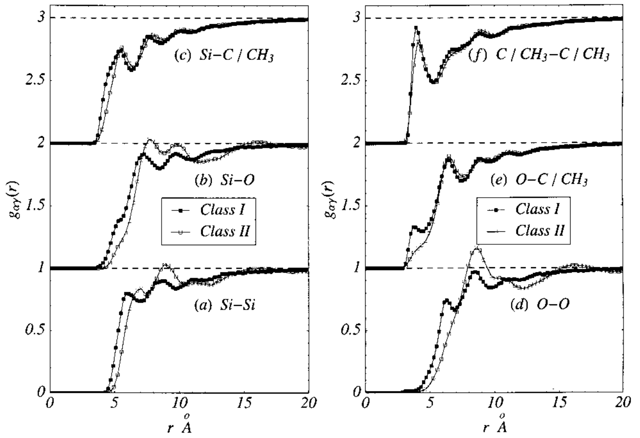

Figure 6. Comparison of intermolecular correlation functions $g_{\alpha,\gamma}(r)$ as calculated from MD simulation using the full UA/CI (filled symbols) and EA/CII (open symbols) potentials for PDMS, including the Coulombic interaction. All data for $\rho =$ 0.98 g/cm^3 and $T = 300$ K.

To provide the most direct test of PRISM, MD simulation data and PRISM are compared in Figure 5 in the case for only repulsive LJ interactions and no Coulombic interactions. It can be seen from these figures that PRISM theory is in good qualitative agreement with the MD simulations for all six intermolecular correlation functions. Because of numerical errors in evaluating PRISM theory, some of the $g_{\alpha,\gamma}(r)$ functions have spurious negative values. As in the case of PIB,[1] the PRISM $g_{\alpha\gamma}(r)$ for PDMS have less structure than those from the MD simulations. In the case of the methyl/methyl correlation functions, the agreement between PRISM and MD is better than was found earlier for PIB. This is likely due to the larger lengths of the Si−O and Si−CH$_3$ bonds that result in a smaller overlapping of sites in the PDMS molecule relative to PIB at the same temperature. A measure of the extent of site overlapping is provided by the ratio of effective hard core diameter d (see Table 1) between sites divided by the bond length l. If there was no site overlap, this ratio would be less than or equal to one. For the Si−O bond $l = 1.60$ Å and $d/l = 1.97$ compared to 2.62 for the corresponding bond in PIB. Likewise, for the Si−CH$_3$ bond $l = 1.88$ Å and $d/l = 1.89$ compared to 2.60 for the C−CH$_3$ bond in PIB. Since PRISM, as well as RISM, theory is known[36] to be less accurate as the site diameters overlap more, one would expect PRISM theory to be more accurate for PDMS than for PIB, and this is what is observed here.

It is interesting to observe in Figure 5 that PRISM theory predicts a small peak in the O−CH$_3$ correlation function at about 3.2 Å, corresponding to the hard core contact distance (see Table 1) between these sites. As can be seen in Figure 4, this peak does not appear in the MD simulation when the site−site interactions are purely repulsive. Since this peak occurs at the same distance scale as the spurious negative values for some of the other $g(r)$ functions, it is likely a consequence of PRISM theory trying to keep the density approximately constant. It can also be observed in Figure 5 that in four of the six pair correlation functions the PRISM theory prediction at short range is shifted to smaller distances relative to MD. Interestingly, when the attractive and Coulombic interactions are turned on, as seen in Figure 4, the MD correlations also shift to smaller distances. In summary, when PRISM theory and simulation are compared using the same site−site potentials, PRISM theory behaves as if the sites are somewhat smaller than they actually are. This characteristic was also seen in earlier studies[1,36] of polyolefins.

Figure 6 compares the $g_{\alpha\gamma}(r)$ functions calculated from MD simulations using the full UA/CI and EA/CII potentials for PDMS, including Coulombic interactions. A direct comparison between each of the 10 correlation functions of the EA/CII model with the six correlation functions of the UA/CI model is not possible. Therefore, Figure 6 shows the six $g_{\alpha\gamma}(r)$ functions for the EA/CII model such that $H \notin \alpha, \gamma$. These $g_{\alpha\gamma}(r)$ functions are compared with the data from the UA/CI model simulations such that if $C \in \alpha, \gamma$ for the EA/CII model, then CH$_3 \in \alpha, \gamma$ for the UA/CI model. Some of the correlation functions are nearly identical such as those in Figure 6c,f while the data in Figure 6a,d have significant differences. For all $g_{\alpha\gamma}(r)$ functions, however, the EA/CII results show a larger first peak which is shifted to larger r due in part to details of the nonbond potential. The form of the EA/CII nonbond potential (eq 11) for the parameters given in Table 2 has a more shallow attractive well and a softer repulsive core for each species than the UA/CI nonbond potential. This also has an effect on the long-range structure.

Long-range structure in the melt can be investigated by studying the Fourier transform of the real-space correlation function which can be compared to the results shown in Figure 3 from WAXS. The scattering intensity

$$I(k) = \sum_{ij}^{N} b_i(k)\, b_j(k) e^{ik(r_i - r_j)} \tag{18}$$

is calculated directly from the particle positions generated from MD simulation and averaged over several configurations. To compare with the experimental data, the scattering intensity is calculated on a per average site basis $H(k)$[37] as defined in eqs 14−16 (section 2.3). The $H(k)$ as calculated from the MD data uses the CH$_3$ scattering form factor for all of the C sites and ignores the direct contribution from the H sites, as done in the experimental analysis.

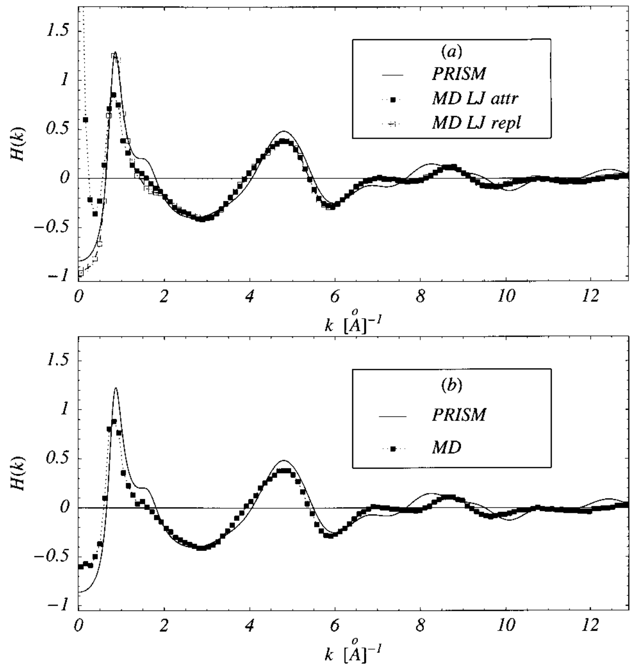

Figure 7. Comparison of $H(k)$ as calculated from MD simulations for the UA/CI model and PRISM theory (solid line) for (a) $\rho = 0.98$ g/cm^3 and (b) $\rho = 1.01$ g/cm^3 at $T = 300$ K. For the MD simulations the symbols denote LJ attractions on (filled squares) and LJ attractions off (open squares). All data have Coulomb interactions turned off.

Results for $H(k)$ from MD and PRISM are shown in Figure 7a,b. To make the most direct comparisons to PRISM, the MD simulations for the UA/CI model are used without Coulomb interactions. The MD data in Figure 7a include one set of data which is obtained using a LJ potential that includes only repulsive interactions and the other which also includes attractive interactions. The agreement between MD with repulsive LJ and PRISM is very good over the entire k range, especially for $k \gtrsim 2$ Å^{-1}. PRISM predicts a small shoulder near the main peak located at $k \approx 1$ Å^{-1} that is completely absent in the MD results; however, the height and position of the main peak and $H(k)$ as $k \to 0$ are in excellent agreement.

The agreement between MD using a LJ potential with attractions included and PRISM is also very good for $k \gtrsim 2$ Å^{-1}; however, the low-k behavior shows drastic disagreement with the MD results, showing a huge increase in $H(k)$ as $k \to 0$. This large increase at low k is indicative of a large isothermal compressibility $\kappa_T = -(1/V)(\partial V/\partial P)_T$ since κ_T is related to the zero-k limit of the scattering intensity, eq 17. The behavior of $H(k)$ at low k suggests that this particular UA/CI model for PDMS results in a compressibility that is too large. This is confirmed by direct measurement of the system pressure, shown in Table 3, which is large and negative.

To further investigate this problem with the UA/CI model, both PRISM and MD calculations are performed at a higher density $\rho = 1.01$ g/cm^3, shown in Figure 7b. Increasing the density should have a similar effect as truncating the LJ potential so as to include only repulsive interactions and reduce the compressibility. Figure 7b shows the PRISM calculation and MD simulation data with an attractive LJ interaction for $\rho = 1.01$ g/cm^3. As in Figure 7a, the PRISM and MD data agree well for $k > 2$ Å^{-1}. For the MD data at $\rho = 1.01$ g/cm^3, the large increase in $H(k)$ for small k is suppressed and more closely agrees with PRISM results. The scattering data in Figure 7a,b both show that this particular UA/CI model does not predict the correct phase behavior for PDMS. This anomalous low-k behavior is not a finite-size effect as it persists for larger system sizes. A system with 800 chains (i.e., 8 times the volume of the smaller systems) shows an even larger isothermal compressibility compared to that of the smaller systems. For higher T, the bulk thermodynamic properties become less sensitive to the attractive part of the LJ potential and more sensitive to the repulsive part. Simulations run at $T = 450$ and 600 K at the same density ($\rho = 0.98$ g/cm^3) show that, as $k \to 0$, $H(k)$ decreases with increasing T, similar to the effect of turning off the attractions in the LJ potential seen in Figure 7.

Table 3. Pressure, Mean-Squared Radius of Gyration $\langle R_g^2\rangle$, and End-to-End Distance $\langle R_{ee}^2\rangle$ for the UA/CI Model[a]

q	ρ [g/cm^3]	LJ	P [atm]	$\langle R_g^2\rangle$ [Å^2]	$\langle R_{ee}^2\rangle$ [Å^2]
off	0.98	repl	3135.7 ± 29.2	74.1 ± 0.4	467.9 ± 6.7
off	0.98	attr	−1013.6 ± 47.2	72.4 ± 0.6	439.0 ± 13.7
off	1.01	attr	−1104.0 ± 46.6	71.5 ± 0.5	441.4 ± 6.8
on	0.98	attr	−963.0 ± 35.5	80.6 ± 0.3	498.9 ± 4.4

[a] PRISM calculations using $\rho = 0.98$ g/cm^3 give $\langle R_g^2\rangle = 84.2 \pm 0.6$ and $\langle R_{ee}^2\rangle = 549.0 \pm 8.4$. Note: the pressure values do not include tail corrections.

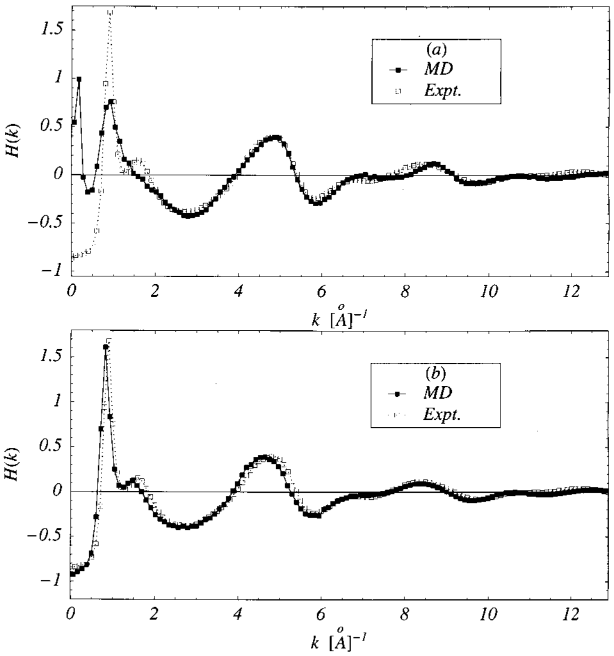

Figure 8. Comparison of $H(k)$ as obtained from WAXS and MD simulations using (a) UA/CI model and (b) EA/CII model. Coulomb and attractive LJ interactions are turned on for MD simulations. The simulations are performed at the experimental density $\rho = 0.98$ g/cm^3 and near the experimental temperature $T = 300$ K ($T_{expt} = 298$ K).

Figure 8a,b compares $H(k)$ as measured from WAXS with results from MD simulations using UA/CI and EA/CII potentials. Figure 8a shows the agreement between the UA/CI model and WAXS is quite good for large k but breaks down drastically for $k \lesssim 2$ Å^{-1}. As for the MD results obtained without Coulomb interactions, the UA/CI model with Coulomb interactions incorrectly predicts the low-k portion of the structure factor. Figure 8b compares the experimental data with the EA/CII

Table 4. Pressure, Mean-Squared Radius of Gyration $\langle R_g^2\rangle$, and End-to-End Distance $\langle R_{ee}^2\rangle$ for the EA/CII Model[a]

ρ [g/cm^3]	P [atm]	$\langle R_g^2\rangle$ [Å^2]	$\langle R_{ee}^2\rangle$ [Å^2]
0.95	−21.1 ± 43.7	90.7 ± 3.8	645.2 ± 49.6
0.98	190.9 ± 53.2	92.6 ± 2.4	672.2 ± 32.3
1.01	575.7 ± 37.2	91.3 ± 2.1	666.9 ± 27.8

[a]Note: the pressure values do not include tail corrections.

potential. Clearly, the agreement over the entire range of k is very good, except for the $H(0)$ limit. The simulation result for the EA/CII potential is $H(0) = -0.920$, which gives a compressibility of $\kappa_T = 0.000\,605$ MPa^{-1}.

The radius of gyration R_g and end-to-end distance R_{ee} of the PDMS chains are listed in Tables 3 and 4 for the UA/CI and EA/CII potentials, respectively. It can be seen from Table 3 that attractions have almost no effect on the radius of gyration as expected for a dense liquid. Turning on the charges, however, leads to a 9% increase in chain dimensions due to intramolecular, Coulombic repulsions. PRISM theory predicts a somewhat larger R_g than observed in the corresponding MD simulations in Table 3. From Table 4 we observe that the EA/CII model predicts significantly higher chain dimensions than from the UA/CI model. These can be compared to $R_{ee}^2 \sim 613$ Å^2 inferred from experiments[38] for long chains in a Θ solvent. Overall, the agreement between R_g and R_{ee} as obtained from MD simulation and PRISM is reasonable and similar to the agreement found in studies of polyolefins.[1]

The system pressure is also listed in Tables 3 and 4. Table 3 contains data for the same model parameters shown in Figure 4, including data for a system at $\rho = 1.01$ g/cm^3. As expected, the pressure in a system without LJ attractions has a large positive pressure. However, a large negative pressure is measured for the UA/CI model when LJ attractions and Coulomb interactions are present. The anomalous low-k behavior for $H(k)$ seen in the simulation data (Figure 8a) is consistent with the large negative pressure at experimental density obtained with the UA/CI potential. In effect, the liquid/gas transition temperature for this particular model is too high. The pressure obtained from simulations using the EA/CII potential for $\rho = 0.98$ g/cm^3 (i.e., near the experimental density) results in a small positive pressure, while for a simulation with $\rho = 0.95$ g/cm^3 (i.e., slightly below the experimental density) gives a small negative pressure. To further test the ability of EA/CII potential to reproduce the correct pressure and density of PDMS, the length of the simulation box in the z-direction is increased, resulting in a liquid/vapor interface in the z-direction, i.e., a “slab” geometry. The PDMS slab is free to adjust its volume and come to a zero pressure state by expanding or contracting in the z-direction. The density in the center of the PDMS slab is in good agreement with bulk simulations, which give a value of $\rho = 0.95$ g/cm^3 for a system with small negative pressure. This value of the density is consistent with the values of $H(k)$ at low k obtained from simulation which slightly underpredict the isothermal compressibility for a system fixed at experimental density. Note, however, that the simulations are for relatively short chains. For longer chains, the density at zero pressure will surely increase toward the experimental value of $\rho = 0.98$ g/cm^3.

IV. Experimental Analysis

The experimental data for $H(k)$ presented in the preceding section can be analyzed further to extract information about the structure of PDMS. The total structure factor, $H(k)$, is a weighted sum of partial structure factors

$$H(k) = M(k)\left[\frac{1}{n_s}\sum_{\alpha\gamma}^{n} b_\alpha b\gamma(\hat{\Omega}_{\alpha\gamma}(k) + \rho_\gamma \hat{h}_{\alpha\gamma}(k)) - S_{\mathrm{self}}(k)\right] \tag{19}$$

where n_s is the number of sites within a monomer (4 in the case of PDMS), $\hat{\Omega}_{\alpha\gamma}(k)$ is the intramolecular, and $\hat{h}_{\alpha\gamma}$ the intermolecular components. Although both the intramolecular and intermolecular structure are of interest, it is the latter which primarily contains information on chain−chain packing in the melt. For polymer chains the intramolecular structure generally overlaps the intermolecular structure, and a unique separation of the two is not possible from a single diffraction experiment. However, there are some intramolecular correlations which can be extracted uniquely from the total structure factor $H(k)$. These correlations are the Si−O and Si−CH$_3$ bond distances (1−2 distances), and the distances between the first and third sites in the bonded triplets (1−3 distances) Si−O−Si, O−Si−O, CH$_3$−Si− CH$_3$, and CH$_3$−Si−O which, together with the bond distances, define the equilibrium bond angles. They are all at distances less than, or minimally overlap, the shortest intermolecular contacts (3 Å, see Figures 4−6). The contribution of these six intramolecular distances to the total intramolecular structure can be approximated by

$$\hat{\omega}_{\alpha\gamma}(k) = w_{\alpha\gamma}\exp(-l_{\alpha\gamma}{}^2k^2/2)\sin(kr_{\alpha\gamma})/(kr_{\alpha\gamma}) \tag{20}$$

where $r_{\alpha\gamma}$ is the mean value and $l_{\alpha\gamma}$ is the rms deviation of an assumed Gaussian distribution for the separation of sites α and γ. The weights $w_{\alpha\gamma}$ specify the number of these correlations. These correlations are also the site−site distances that are approximately independent of molecular conformation—all other intramolecular distances (1−4 and higher) depend on the conformation of the polymer chain (i.e., bond torsions).

The dominant oscillations in $H(k)$ above $k \sim 2$ Å^{-1} (see Figure 9) are due to these shortest intramolecular correlations. We construct a partial structure factor $H_m(k)$ based on these shortest correlations by summing over the sites involving only 1−2 and 1−3 distances in eq 20. The parameters $w_{\alpha\gamma}$, $r_{\alpha\gamma}$, and $l_{\alpha\gamma}$ are obtained by a least-squares refinement against the k-weighted total structure factor $kH(k)$ from $k = 2$ to 16 Å^{-1}. This model structure factor, $H_m(k)$, is shown in Figure 9a together with the experimental total structure factor $H(k)$. The difference, $H_d(k)$, is shown in the lower part of Figure 9a. Twofold symmetry for the Si center was assumed in the fit. This fitting procedure was also applied to the $kH(k)$ data generated from the MD simulations for the EA/CII model, which is compared to the experimental k-weighted structure factor in Figure 9b. The bond distances and bond angles obtained in this way from the X-ray and MD data are listed in Table 5.

In Figure 9 we show these functions weighted by k for several reasons. First, it is $kH(k)$ that appears in the kernel of the Fourier transform for the radial distribution function (see below), and it can be seen that

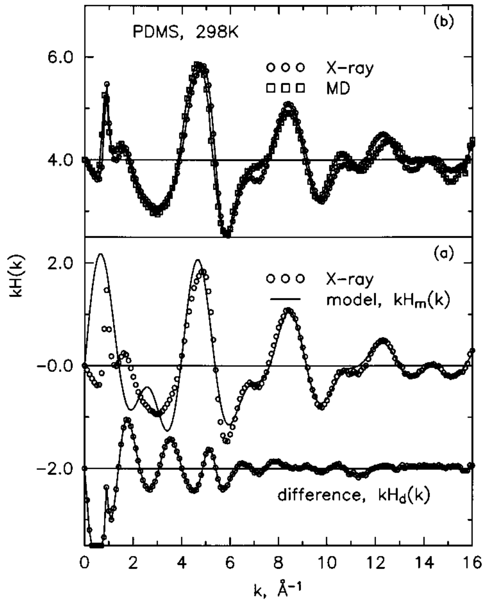

Figure 9. (a) The *k*-weighted total structure factor $kH(k)$ and the model structure factor $kH_m(k)$, top; the difference structure factor $kH_d(k)$, bottom. (b) Comparison between the *k*-weighted total structure factor $kH(k)$ from MD simulation and experiment. Results of the least-squares analysis used to determine the six intramolecular correlation distances in $H_m(k)$ are shown in Table 5.

Table 5. Results for the Short-Range Intramolecular Structure by Fitting the *k*-Weighted Total Structure Factor *kH*(*k*) from WAXS Experiment and MD Simulation (See Figure 9)[a]

correlations	X-ray (fit)	MD (fit)	MD (direct)	class II potential
		Bond Distance r (Å)		
Si−O	1.626 (0.005)	1.647 (0.003)	1.634 (0.0002)	1.64
Si−CH$_3$	1.836 (0.008)	1.907 (0.005)	1.894 (0.0002)	1.899
		Bond Angle (deg)		
O−(Si)−O	105.9 (1.40)	107.4 (1.20)	107.86 (0.02)	110.7
CH$_3$−(Si)−O	110.4 (0.90)	110.0 (0.60)	110.77 (0.03)	114.90
CH$_3$−(Si)−CH$_3$	109.5[b]	109.5[b] fixed	109.30 (0.01)	113.19
Si−(O)−Si	149.6 (1.20)	146.7 (0.90)	147.50 (0.06)	159.0

[a] The angles are also directly measured from the MD simulation. Note that the angles are renormalized from the EA/CII potential due to condensed phase effects. The standard deviations in the measurements are shown in parentheses. [b] This value was fixed in the least-squares analysis.

the $kH(k)$ amplitude in the high-k region is large and contributes appreciably to the transform. Second, it shows that the *k*-weighted functions have appreciable amplitude beyond $k = 16$ Å^{-1}, which will result in a truncation error in the Fourier transform. These considerations suggest that this function could be measured to higher momentum transfer values with synchrotron radiation, for example. Third, it shows that one must obtain good statistics at high k values (compare to Figures 2 and 3), if one wants to retain good statistics in the difference function $kH_d(k)$. For the experimental data this means accumulating a very high number of counts in this region (as many as 10^6), where the count rate is lowest. For the simulation data this corresponds to sampling many chain configurations as well as using a large number of *k*-vectors in the structure factor analysis. Note that all parameters in Table 5 have been obtained from a fit in *k*-space; therefore, the analysis does not depend on the transformed data.

In Table 5, the Si−O and Si−CH$_3$ bond lengths obtained from the least-squares analysis are compared to the equilibrium bond distances defined by the EA/CII potential. It can be seen that the bond lengths used in the EA/CII potential, and found in the MD simulations, are close to but slightly larger than the experimentally measured values. The Si−O and Si−CH$_3$ distances of 1.626 and 1.836 Å extracted from our experimental data compare favorably with the 1.630 and 1.857 Å interatomic distances given in a compilation derived from many organic crystals.[39]

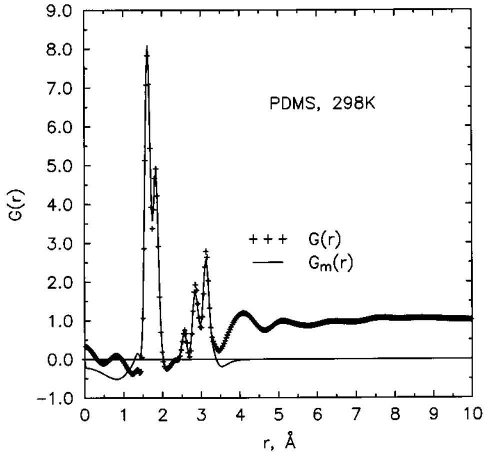

Figure 10. Total experimental radial distribution function $G(r)$ and the model distribution function $G_m(r)$.

An interesting effect emerges when one examines the angles deduced from experiment and the simulation. By comparing column 5 with columns 3 and 4 in Table 5, one observes that the bond angles from the EA/CII potential get renormalized due to condensed phase effects. In other words, the bond angles of an isolated PDMS chain, in a hypothetical gas phase, change rather dramatically when that molecule is inserted into a dense liquid of other PDMS chains. It can be seen that this condensed phase effect is accounted for rather well in the MD simulations by comparing columns 3 and 4 with the corresponding experimentally deduced angles in column 2. It can be observed that the Si−O−Si angle exhibits the largest condensed phase effect. This is not be surprising since this angle also has the weakest force constant for bending in the EA/CII potential.

The total radial distribution function $G(r)$ is obtained from the Fourier transform of the structure factor

$$G(r) = 1 + (2\pi^2\rho r)^{-1}\int_0^\infty kH(k)\,\sin(kr)\,\mathrm{d}k \qquad (21)$$

It is well-known that the finite upper limit ($k_{\max} = 16$ Å^{-1}) in this integral introduces certain truncation errors in the $G(r)$. However, since the model structure factor $kH_m(k)$ closely approaches the experimental structure factor $kH(k)$ at high k values, as shown by the fit and the difference curve $kH_d(k)$ in Figure 9a, it can be used to extend the experimental structure factor beyond $k_{\max} = 16$ Å^{-1} to arbitrary values and thus avoid the truncation error in the Fourier transform. Thus, eq 21 can be used to transform the extended experimental structure factor to real space. It should be pointed out, however, that the resulting $G(r)$ is not purely a structural correlation function since it depends on the specific values of the site scattering factors $b_\alpha(k)$ folded into $H(k)$. The $G(r)$, as well as the transform of the model representing the short intramolecular correlations, $G_m(r)$, is shown in Figure 10. The two bond lengths and the triplet distances are clearly separated from the rest

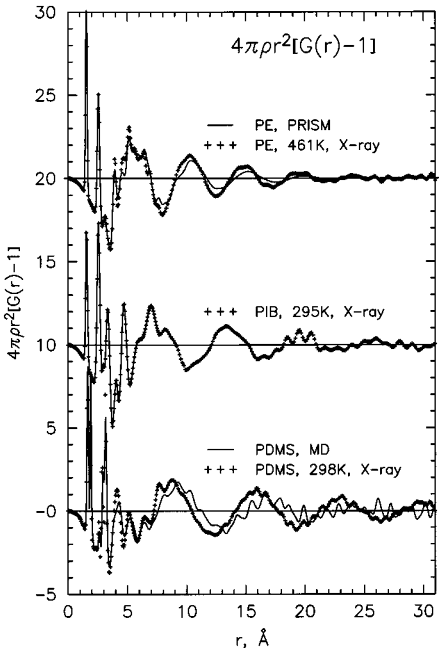

Figure 11. Experimental r^2-weighted radial distribution function $G(r)$ for PE, PIB, and PDMS. PRISM calculations for PE and MD simulations for PDMS from this work are also shown. The curves for PE and PIB are offset for clarity.

of the $G(r)$ and are well represented by the short-range intramolecular model structure, $G_m(r)$.

In the above analysis we have extracted the intramolecular information unambiguously accessible from the total experimental structure factor. Let us now turn to the remaining $G(r)$ above 3.5 Å, which exhibits a series of features that decay to small values at $r \sim 8$ Å (Figure 10). To better display this region and beyond, we show the r^2-weighted experimental $G(r)$ in Figure 11, together with those of polyethylene (PE) and PIB. All three polymers show regular, low-frequency oscillations to long distances in $G(r)$ ~20 Å for PE, ~26 Å for PIB, and at least to ~31 Å for PDMS. Beyond the sharp, short-range, intramolecular features, the oscillations arise largely from intermolecular correlations. These substantial oscillations are not at all obvious in the unweighted representation $G(r)$. The period of the oscillations is about 4.5 Å for PE, 6.1 Å for PIB, and 7.1 Å for PDMS. Clearly, for these polymers the periods track the thickness of the chains. These oscillations are reminiscent of the packing of simple atomic liquids, where they represent nearest-neighbor, next-nearest-neighbor, etc., correlations. Such atomic fluids are well represented by hard-sphere fluids. In analogy, the $G(r)$ for these polymers might be interpreted, to first order, in terms of flexible hard cylinder fluids, where the oscillations represent the nearest-neighbor, next-nearest-neighbor, etc., cylinder−cylinder (chain−chain) correlations. In this view the $G(r)$ should track the thickness of the chains, independent of the details of the chain structure. This interpretation is not a trivial result, since such regularity in $G(r)$ is not always the case. The r^2-weighted $G(r)$ of isotactic polypropylene is almost devoid of these oscillations,[2] and poly(1-butene) (P1B) and poly(4-methyl-1-pentene) (PMP) show complex behavior.[40] In the case of P1B and PMP, this implies chain packing more complex than simple hard cylinder packing.

Finally, in Figure 11, we compare the total $G(r)$ obtained from PRISM calculations for PE[36] and the MD results in this work for PDMS. In both cases the oscillations and the periods are reasonably well reproduced.

V. Conclusion

In the present investigation we made detailed comparisons between MD simulations, PRISM theory, and WAXS experiments on PDMS. Our objective was to evaluate the adequacy of current UA/CI and EA/CII models to predict the structural properties of PDMS chains in the melt state. Our main conclusions can be summarized as follows:

1. With the UA/CI model, attractive interactions have a larger than expected effect on the intermolecular pair correlation functions. The additional structure observed when attractions are turned on may be due to the rather large Lennard-Jones attractions in the UA/CI model as seen in Table 1 compared to the corresponding parameters in the EA/CII model listed in Table 2,
2. In the UA/CI model, Coulombic charges are seen to significantly increase the short-range structure in the O−O, O−CH_3, and Si−Si correlation functions.
3. PRISM theory is in good qualitative agreement with MD simulations for PDMS,
4. The UA/CI model predicts significantly more short-range structure than the EA/CII model.
5. The EA/CII model is in very good agreement with WAXS measurements of PDMS at 298 K.
6. The UA/CI model is in poor agreement with WAXS measurements on PDMS at low wave vector, a consequence of this particular UA/CI model's inability to capture the correct *PVT* properties.

The fact that the particular UA/CI model used here[3] is inadequate for predicting the structure of PDMS melts does not necessarily imply that a united atom model, in which the CH_3 group is represented as a single site, will not work for PDMS. Indeed, our earlier success[1] in using a united atom model to describe polyisobutylene suggests that it should also be possible to develop an accurate united atom model for PDMS.

Acknowledgment. This work was supported in part by the DOE Office of Science through the Computational Materials Science Network. Sandia is a multiprogram laboratory operated by Sandia Corporation, a Lockheed Martin Company, for the United States Department of Energy under Contract DE-AC04-94AL85000. Experimental research sponsored by the Division of Chemical Sciences, Geosciences, and Biosciences, Office of Basic Energy Sciences, U.S. Department of Energy, under Contract DE-AC05-00OR22725 with Oak Ridge National Laboratory, managed and operated by UT-Battelle, LLC.

References and Notes

(1) Pütz, M.; Curro, J. G.; Grest, G. S. *J. Chem. Phys.* **2001**, *114*, 2847.
(2) Weinhold, J.; Curro, J.; Habenschuss, A.; Londono, J. *Macromolecules* **1999**, *32*, 7276.
(3) Sok, R. M.; Berendsen, H. J. C. *J. Chem. Phys.* **1992**, *96*, 4699.
(4) Hwang, M. J.; Stockfisch, T. P.; Hagler, T. A. *J. Am. Chem. Soc.* **1993**, *116*, 2515.
(5) Maple, J. R.; Hwang, M. J.; Stockfish, T. P.; Dinur, U.; Waldman, M.; Ewig, C. S.; Hagler, A. T. *J. Comput. Chem.* **1994**, *15*, 162.
(6) Sun, H. *Macromolecules* **1995**, *28*, 701.
(7) Sun, H.; Rigby, D. *Spectrochim. Acta, Part A* **1997**, *53*, 1301.
(8) Sun, H. *J. Phys. Chem. B* **1998**, *102*, 7338.
(9) Schweizer, K.; Curro, J. *Phys. Rev. Lett.* **1987**, *58*, 246.

(10) Curro, J.; Schweizer, K. *Macromolecules* **1987**, *20*, 1928.
(11) Curro, J.; Schweizer, K. *J. Chem. Phys.* **1987**, *87*, 1842.
(12) Chandler, D.; Andersen, H. *J. Chem. Phys.* **1972**, *57*, 1930.
(13) Chandler, D. In *Studies in Statistical Mechanics VIII*; Montroll, E., Lebowitz, J., Eds.; North-Holland: Amsterdam, 1982.
(14) Schweizer, K.; Curro, J. *Adv. Polym. Sci.* **1994**, *116*, 321.
(15) Schweizer, K.; Curro, J. *Adv. Chem. Phys.* **1997**, *98*, 1.
(16) Hansen, J.; McDonald, I. *Theory of Simple Liquids;* Academic Press: London, 1986.
(17) Weeks, J.; Chandler, D.; Anderson, H. *J. Chem. Phys.* **1971**, *54*, 5237.
(18) Rajasekaran, J.; Curro, J.; Honeycutt, J. *Macromolecules* **1995**, *28*, 6843.
(19) Clancy, T. C.; Pütz, M.; Weinhold, J.; Curro, J.; Mattice, W. *Macromolecules* **2000**, *33*, 9452.
(20) Flory, P. *J. Chem. Phys.* **1949**, *17*, 203.
(21) Chandler, D.; Singh, Y.; Richardson, D. *J. Chem. Phys.* **1984**, *91*, 1975.
(22) Nichols, A.; Chandler, D.; Singh, Y.; Richardson, D. *J. Chem. Phys.* **1984**, *81*, 5109.
(23) Hockney, R.; Eastwood, J. *Computer Simulation using Particles;* Adam Hilger: New York, 1988.
(24) Even though the MD simulations were run for $N = 20$ monomers, the experimental polymer density ($\rho = 0.98$ g/cm^3 at 298 K) is used to make a more realistic comparison with wide-angle X-ray scattering data which is known to have a weak molecular weight dependence.
(25) "Aldrich Fine Chemicals, Catalog 1998−99", p 1356, product no. 18,183-8.
(26) Cullity, B. *Elements of X-ray Diffraction;* Addison-Wesley: Reading, MA, 1956.
(27) Narten, A.; Habenschuss, A.; Honnell, K.; McCoy, J.; Schweizer, K. *J. Chem. Soc., Faraday Trans.* **1992**, *88*, 1791.
(28) Levy, H.; Agron, P.; Danford, M. *J. Appl. Phys.* **1959**, *30*, 2012.
(29) Cromer, D.; Mann, J. *J. Chem. Phys.* **1967**, *47*, 1893.
(30) Narten, A.; Levy, H. In *Water: A Comprehensive Treatise*; Franks, F., Ed.; Plenum: New York, 1972.
(31) Warren, B.; Mozzi, R. *Acta Crystallogr.* **1966**, *21*, 459.
(32) In *International Tables of X-Ray Crystallography*; Ibers, J. A., Hamilton, W. C., Eds.; Kynoch: Birmingham, 1974; Vol. IV, Chapter 2.2.
(33) Narten, A. H. *J. Chem. Phys.* **1979**, *70*, 299.
(34) Guinier, A. In *X-ray Diffraction*; W.H. Freeman: San Francisco, 1963; Chapter 2.
(35) Zoller, P.; Walsh, D. In *Standard Pressure−Volume−Temperature Data for Polymers*; Technomic Publ.: Lancaster, PA, 1995.
(36) Curro, J. G.; Webb, E. B., III.; Grest, G. S.; Weinhold, J. D.; Pütz, M.; McCoy, J. D. *J. Chem. Phys.* **1999**, *111*, 9073.
(37) Londono, J. D.; Habenschuss, A.; Curro, J. G.; Rajasekaran, J. J. *J. Polym. Sci., Part B: Polym. Phys.* **1996**, *34*, 3055.
(38) Flory, P. *Statistical Mechanics of Chain Molecules;* Interscience: New York, 1969.
(39) Lide, D. R.; Frederikse, H. *CRC Handbook of Chemistry and Physics;* CRC Press: Boca Raton, FL, 1994.
(40) Kim, M. H.; Habenschuss, A., unpublished data.

MA020014K